

H I Kinematics and the E(B-V)/N(H I) ratio

HARVEY LISZT¹

¹*National Radio Astronomy Observatory
520 Edgemont Road, Charlottesville, VA 22903
hliszt@nrao.edu*

ABSTRACT

The $\lambda 21\text{cm}$ H I emission that is used to trace the gas to dust ratio at high Galactic latitudes has contributions from material beyond the Milky Way disk, with uncertain and likely sub-Solar metallicity and dust content. These contributions can be isolated kinematically and their presence is clear for sightlines with small mean reddening $\langle E(B-V) \rangle \lesssim 0.03$ mag, which have mean ratios $\langle N(\text{H I}) \rangle / \langle E(B-V) \rangle$ that are 20-50% above the high latitude Galactic average $\langle N(\text{H I}) \rangle / \langle E(B-V) \rangle = 8.3 \times 10^{21} \text{cm}^{-2} \text{mag}^{-1}$. By mapping N(H I) and E(B-V) across H I High Velocity Cloud complexes and the Magellanic Clouds we show that the reddening of this kinematically-isolated gas is on average five times smaller per H I than the high latitude average. However, the aggregate contribution of this gas is small and $\langle N(\text{H I}) \rangle / \langle E(B-V) \rangle = 8.3 \times 10^{21} \text{cm}^{-2} \text{mag}^{-1}$ is the appropriate value for Galactic gas seen at high latitude using the H I and reddening measures employed here and in our previous work.

Keywords: astrochemistry . ISM: dust . ISM: H I. ISM: clouds

1. INTRODUCTION

The gas/dust ratio $N(\text{H})/E(B-V)$ is an important benchmark but its measured value is sensitive to context and technique. Two significantly different values are derived from broad swaths of data respectively sampling gas in UV absorption toward early-type stars and gas seen in $\lambda 21\text{cm}$ H I emission from the diffuse interstellar medium in other directions.

When the atomic and molecular constituents of $N(\text{H}) = N(\text{H I}) + 2N(\text{H}_2)$ are measured in UV absorption toward early-type stars and compared with the associated photometric stellar reddening there is a tight relationship $N(\text{H})/E(B-V) =$

$6.1 - 6.2 \pm 0.3 \times 10^{21} \text{cm}^{-2} \text{mag}^{-1}$ (Liszt & Gerin 2023; Shull & Panopoulou 2024) very much like that first determined by Bohlin et al. (1978), $\langle N(\text{H}) \rangle / \langle E(B-V) \rangle = 5.8 \times 10^{21} \text{cm}^{-2} \text{mag}^{-1}$ using *Copernicus*.

The atomic gas/dust ratio $N(\text{H I})/E(B-V)$ should be an equivalent measure at small reddening $E(B-V) \lesssim 0.08$ mag where the molecular gas fraction is negligible (Bohlin et al. 1978), and indeed (Table 2 of Liszt & Gerin (2023)), $\langle N(\text{H I}) \rangle / \langle E(B-V) \rangle = 6.2 \times 10^{21} \text{cm}^{-2} \text{mag}^{-1}$ with N(H I) measured in Lyman- α absorption and compared with stellar photometry. But the scatter in individual stellar measurements is large owing to errors in the photometric reddening, and the average merges a very small value $\langle N(\text{H I}) \rangle / \langle E(B-V) \rangle = 4.1 \times 10^{21} \text{cm}^{-2} \text{mag}^{-1}$ measured by the *Copernicus*

mission with larger values $\langle N(\text{H I}) \rangle / \langle E(\text{B-V}) \rangle \approx 6.9 \times 10^{21} \text{ cm}^{-2} \text{ mag}^{-1}$ measured subsequently toward three times more stars by [Diplas & Savage \(1994\)](#) and [Gillmon et al. \(2006\)](#).

In any case, the above-quoted $N(\text{H})/E(\text{B-V})$ and $N(\text{H I})/E(\text{B-V})$ ratios measured toward stars are significantly smaller than the global low-reddening Galactic average $\langle N(\text{H I}) \rangle / \langle E(\text{B-V}) \rangle = 8.3 - 8.8 \times 10^{21} \text{ cm}^{-2} \text{ mag}^{-1}$ ([Liszt 2014a,b](#); [Lenz et al. 2017](#); [Shull & Panopoulou 2024](#)) that is obtained when $N(\text{H I})$ is measured in $\lambda 21\text{cm}$ H I emission and compared with reddening equivalents derived at far infrared ([Schlegel et al. 1998](#)) or sub-mm ([Planck Collaboration XLVIII et al. 2016](#)) wavelengths. The difference may be related to the viewing geometries. The small scale heights of early-type stars constrain foreground absorbing material to the vicinity of the Galactic plane, where low reddening can occur along short sightlines or along sightlines having a low mean density of intervening material (as was the case for *Copernicus*). By contrast, the low-reddening sightlines observed in $\lambda 21\text{cm}$ H I emission occur only at higher Galactic latitudes and preferentially sample material further from the plane. As a result, the H I line profile integral at higher latitudes samples phenomena like high velocity clouds (HVC) ([Verschuur 1975](#)) that do not occur near the Sun or in the Galactic disk.

This raises the question whether the elevated gas/dust ratios observed at high Galactic latitudes arise through destruction or stripping of dust in disk material ([Draine & Salpeter 1978](#); [Seab & Shull 1983](#); [Hensley & Draine 2021](#)) or from the presence of an admixture of low-reddening external gas. Addressing this question, [Shull & Panopoulou \(2024\)](#) recently showed that inhomogeneities in the composition of the high latitude gas are manifested in variation of the gas/dust ratio with gas velocity. They performed a hybrid measurement of $N(\text{H}_2)$ in UV absorption toward QSO in combination with $N(\text{H I})$ measured in $\lambda 21\text{cm}$ H I emission and $E(\text{B-V})$ taken from the FIR and sub-mm derived reddening equivalents

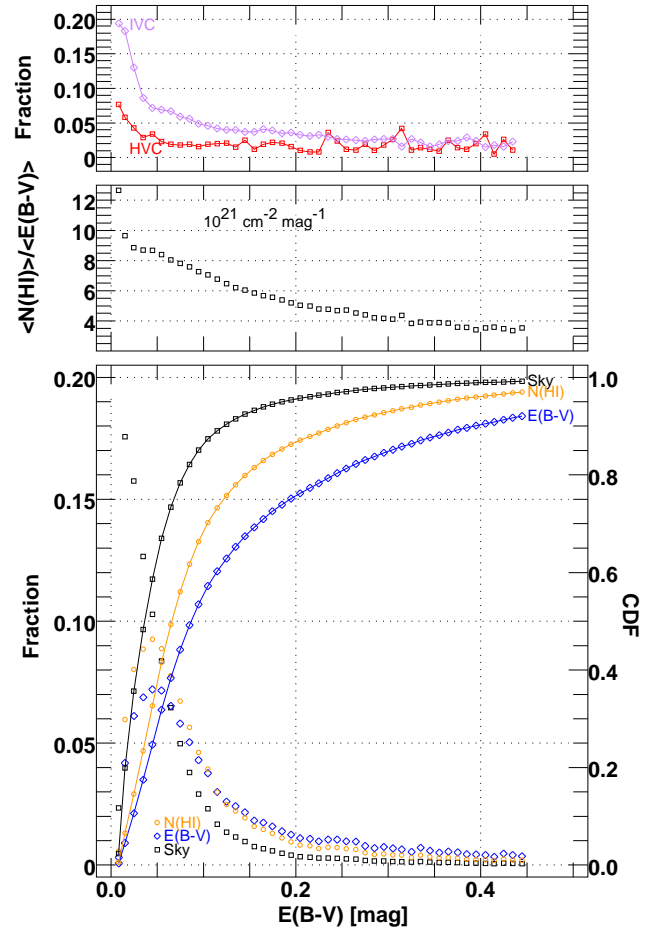


Figure 1. Mean properties of the sky at $|b| > 20^\circ$ binned in 0.01 mag increments of $E(\text{B-V})$. Top: Fraction of $N(\text{H I})$ in HVC at $|v_{\text{lsr}}| > 90 \text{ km s}^{-1}$ and IVC at $30 \text{ km s}^{-1} < |v_{\text{lsr}}| < 90 \text{ km s}^{-1}$. Middle: $\langle N(\text{H I}) \rangle / \langle E(\text{B-V}) \rangle$. Bottom: distribution and cumulative distribution function (CDF) of the fraction of the sky, fraction of the reddening and fraction of the $N(\text{H I})$ binned in $E(\text{B-V})$.

cited above. In this way, they showed (their Table 7) that 9 low-reddening sightlines with relatively large contributions to $N(\text{H I})$ from gas at high negative velocity $v_{\text{lsr}} < -90 \text{ km s}^{-1}$ had elevated $\langle N(\text{H I}) \rangle / \langle E(\text{B-V}) \rangle = 17 \times 10^{21} \text{ cm}^{-2} \text{ mag}^{-1}$ in directions toward HVC Complex C ([Verschuur 1975](#)). They suggested that the HVC gas was material with low metallicity, small dust content and reddening.

Such is the point of departure for the present work, which considers the extent to which the high-latitude gas/dust ratio derived from $\lambda 21\text{cm}$

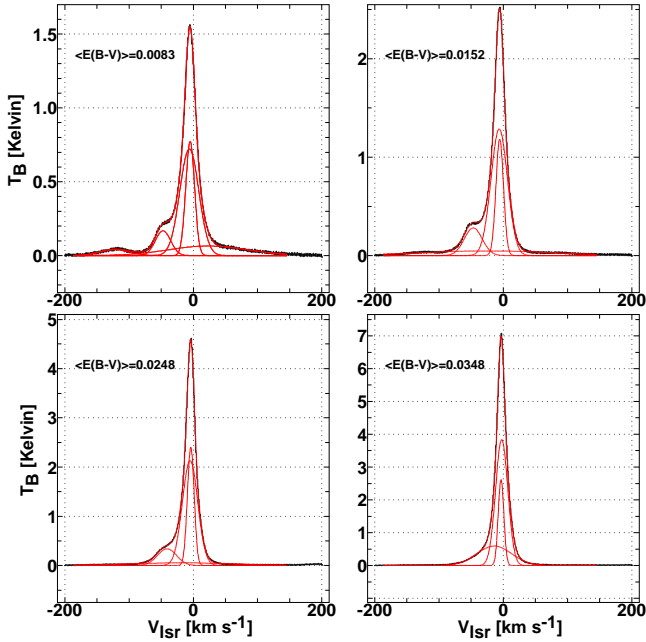


Figure 2. Mean $\lambda 21\text{cm}$ H I brightness profiles for the four lowest-extinction bins shown in Figure 1 with overlaid Gaussian decomposition.

emission is affected by the inclusion of gas seen in emission outside the velocity range associated with Galactic rotation and material in the Galactic disk. Section 2 is a very brief summary of our data sources and methods. Section 3 is the actual discussion and Section 4 is a summary.

2. DATA SOURCES AND CONVENTIONS

2.1. $\lambda 21\text{cm}$ H I emission

As the issue addressed here is the influence of low metallicity gas on our previous determination of $N(\text{H I})/E(B-V)$ (Liszt 2014a,b), we again use the Leiden/Argentine/Bonn (LAB) all-sky H I survey (Kalberla et al. 2005) with 0.6° angular resolution on a uniform 0.5° grid in Galactic coordinates.

As before, H I column densities were derived assuming a spin temperature $T_{\text{sp}} = 145$ K. The $\lambda 21\text{cm}$ optical depth τ was derived from the observed brightness temperature

$$T_{\text{B}} = T_{\text{sp}}(1 - \exp(-\tau))$$

with $T_{\text{sp}} = 145$ K and column densities $N(\text{H I})$ were computed from the fundamental physical relation-

ship for the optical depth of the $\lambda 21\text{cm}$ line

$$\tau = (dN(\text{H I})/dv)/(1.823 \times 10^{18} \text{ cm}^{-2} T_{\text{sp}})$$

with velocity in units of km s^{-1} (Spitzer 1978).

2.2. $E(B-V)$

Also as before, and for the sake of consistency, we use the FIR-derived reddening equivalents of Schlegel et al. (1998). As discussed by Shull & Panopoulou (2024) and as pointed out somewhat more obscurely by Liszt (2021), the overall scale of the reddening derived from the best representation of the 353 GHz Planck dust opacity measurements (Planck Collaboration XLVIII et al. 2016) agrees within about 3% with the work of Schlegel et al. (1998) and not nearly so well with the later upward revision by a factor 1/0.86 recommended by Schlafly & Finkbeiner (2011).

3. $N(\text{H I})$, $E(B-V)$ AND V_{LSR}

Plots of $N(\text{H I})$ against $E(B-V)$ in Liszt (2014a,b) show a very tight linear relationship $N(\text{H I})/E(B-V) = 8.3 \times 10^{21} \text{ cm}^{-2} \text{ mag}^{-1}$ at $0.01 \lesssim E(B-V) \lesssim 0.08$ mag without an indication that $N(\text{H I})$ is being undersampled at the lowest $E(B-V)$ due for instance to the presence of a noticeable proportion of ionized hydrogen.

In such work, low-reddening sightlines are only found at high Galactic latitudes and Figure 1 here explores the high latitude $N(\text{H I})$ - $E(B-V)$ relationship in more detail. We averaged H I line profiles in 0.01 mag bins of $E(B-V)$ at $|b| \geq 20^\circ$ and separated out the kinematic contributions of the so-called high-velocity ($|V_{\text{LSR}}| \geq 90 \text{ km s}^{-1}$; HVC) and intermediate-velocity clouds ($30 \leq |V_{\text{LSR}}| \leq 90 \text{ km s}^{-1}$; IVC) following Wakker (2001). The middle panel shows that sightlines in the bins with $\langle E(B-V) \rangle \leq 0.02$ mag have higher gas/dust ratios $\langle N(\text{H I})/E(B-V) \rangle = 10\text{--}13 \times 10^{21} \text{ cm}^{-2} \text{ mag}^{-1}$ and (upper panel) high proportions of gas at velocities characteristic of HVC.

The numerical values of the distributions plotted in Figure 1 are given in the Appendix. The two

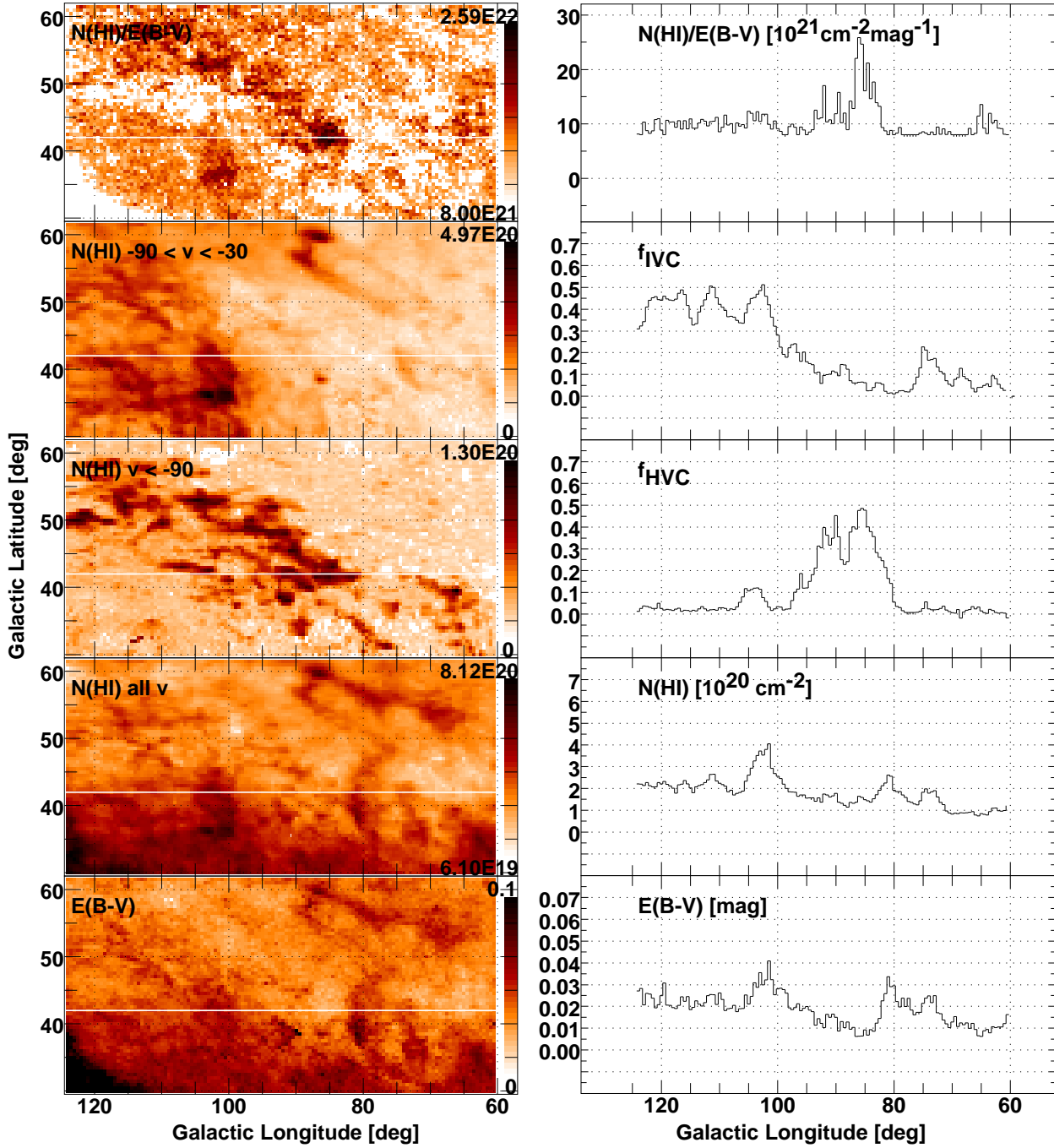


Figure 3. Properties of the sky over the region of HVC Complex C. Left top: $N(\text{HI})/E(\text{B-V})$ scaled and clipped over the range $8 - 25 \times 10^{21} \text{ cm}^{-2} \text{ mag}^{-1}$. Left middle three panels: $N(\text{HI})$ integrated over velocity ranges indicated in each panel. Left bottom: $E(\text{B-V})$ scaled and clipped over the range $0 - 0.1$ mag. Right: Properties along the indicated longitude strip at $b=42^\circ$ for the associated property mapped at left, where f_{HVC} is the fraction of the integrated H I profile at $v_{\text{lsr}} < -90 \text{ km s}^{-1}$ and f_{IVC} is the fraction in the velocity interval $-90 < v_{\text{lsr}} < -30 \text{ km s}^{-1}$.

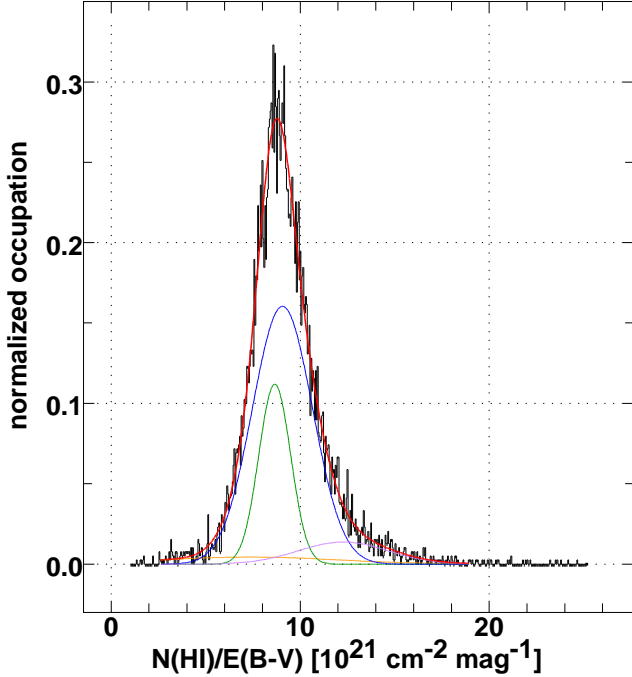


Figure 4. The distribution of reddening over the region shown in Figure 3, decomposed into several gaussian components.

lowest bins represent fractions 0.023 and 0.176 of the sampled sky, fractions 0.006 and 0.060 of the total $E(B-V)$ and fractions 0.003 and 0.042 of the aggregate $N(\text{H I})$. The HVC gas fraction asymptotically achieves a value of 2% for $\langle E(B-V) \rangle > 0.05$ mag. The mean $\lambda 21\text{cm}$ H I emission profiles in the lowest 4 bins of $E(B-V)$ are shown in Figure 2 where it is seen that the contribution of HVC gas is hard to distinguish for $\langle E(B-V) \rangle > 0.03$ mag where the emission around zero velocity is stronger.

The combined fractions of gas in HVC and IVC are 20-25% in the lowest two bins but are too small overall to be responsible for the 40% higher value of $N(\text{H I})/E(B-V)$ seen at high latitude (ie the multipliers 8.3 vs 6.2). This implies that stripping or destruction of dust in Galactic disk gas at large z -heights is responsible, but the kinematic information in the H I profile nevertheless contains information that can be exploited to refine the appropriate high-latitude average gas/reddening ratios for the disk and high-velocity gas.

Figure 3 at left shows properties of the sky over a large region containing HVC Complex C (see also Shull & Panopoulou (2024)). The HVC gas column density in the middle panel is clearly associated with an elongated region of high $N(\text{H I})/E(B-V)$ at top that is not apparent in the maps of $E(B-V)$ and integrated $N(\text{H I})$ at bottom. A small region of high $N(\text{H I})/E(B-V)$ in the top left near $(l,b) = (102^\circ, 37^\circ)$ is associated with a region of high IVC gas column density. Overall the IVC gas is not strongly deficient in $E(B-V)$ and the velocity boundary between HVC and IVC gas is only loosely defined.

Figure 3 at right shows small-scale behaviour along longitude strips at $b=42^\circ$ for each of the properties mapped at left, replacing the HVC and IVC column densities by the fractions of the integrated H I line profile (H I column density) that reside in the HVC and IVC components. The coincident minimum in $E(B-V)$ and maximum in the HVC fraction at $l = 85^\circ$ combine to produce a narrow region of very high $N(\text{H I})/E(B-V)$. The strongly-varying IVC fraction has little effect on the $N(\text{H I})/E(B-V)$ ratio, suggesting that its metallicity and dust/gas content are similar to the Galactic average at these latitudes.

The overall character of the reddening in the region of HVC Complex C is shown in Figure 4 where the distribution of values of $N(\text{H I})/E(B-V)$ is decomposed into gaussian components. In this view the bulk of the gas has $N(\text{H I})/E(B-V) = 8 - 9 \times 10^{21} \text{ cm}^{-2} \text{ mag}^{-1}$ with a small admixture in a broad component centered at $12 \times 10^{21} \text{ cm}^{-2} \text{ mag}^{-1}$. Smaller values of $N(\text{H I})/E(B-V)$ are associated with the higher-reddening region at the lower left corner of map nearer the Galactic plane.

The variation of $N(\text{H I})/E(B-V)$ over the region of high HVC gas fraction at $l=100 - 115^\circ$ in Figure 3 at right somewhat complicates a simple picture where the $N(\text{H I})/E(B-V)$ ratio is determined by a weighted average of disk gas with high metallicity and dust content and an HVC component with low metallicity and near-zero reddening. Nonetheless,

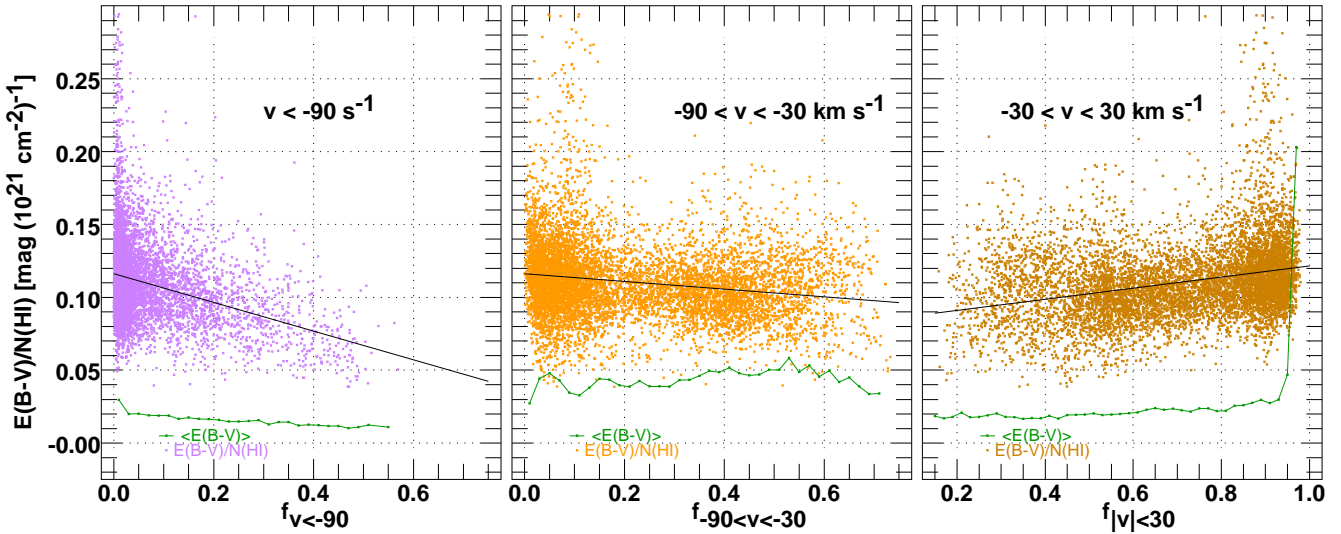


Figure 5. $E(B-V)/N(\text{H I})$ at individual pixels over the region of the HVC Complex C illustrated in Figure 3, plotted against the fraction of the total integrated brightness in three velocity ranges. The solid line in each panel is a least-squares regression fit and the green line is the mean reddening at each value of the fraction along the horizontal axis.

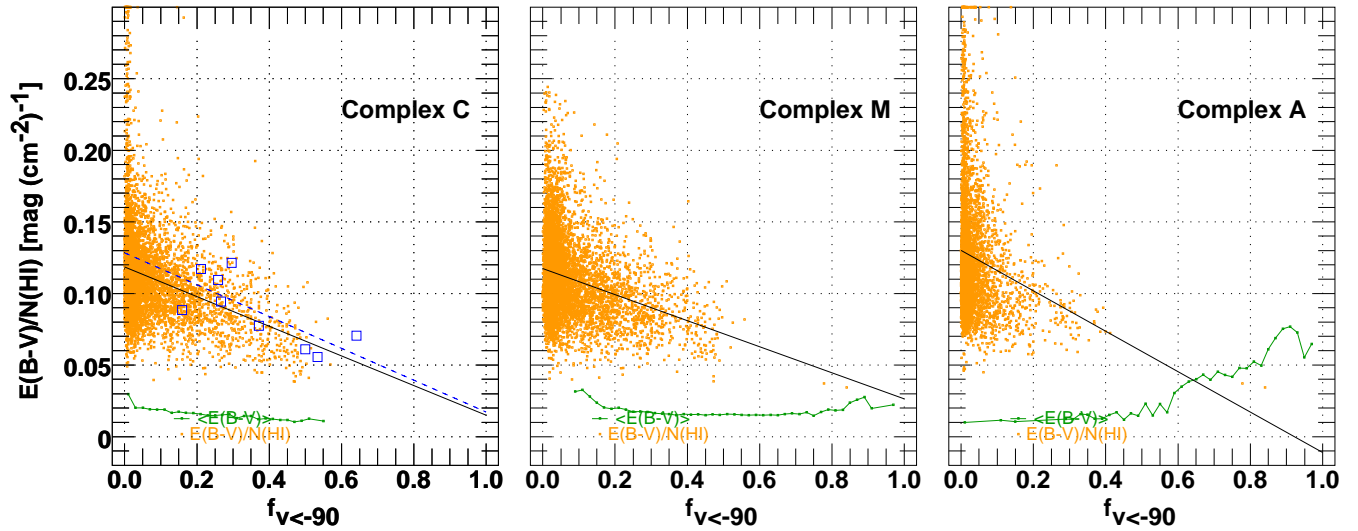


Figure 6. As in the left-most panel of Figure 5, but over an extended range of the H I fraction for three HVC complexes. Blue rectangles and the blue dashed regression line in the left-most panel represent the $E(B-V)/N(\text{H I})$ ratios derived using 353 GHz Planck dust opacity measurements (Planck Collaboration XLVIII et al. 2016) by Shull & Panopoulou (2024) (see their Table 7).

it does appear that the HVC gas on average contributes very little reddening. Shown in Figure 5 are plots of the reddening per atom $E(B-V)/N(\text{H I})$ (both total, $N(\text{H I})$ is the entire profile integral in each case) as it varies with the fractions of the integrated emission or column density in the HVC, IVC and disk ($|v_{\text{lsr}}| \leq 30 \text{ km s}^{-1}$) gas components.

The mean reddening per H I declines sharply with the HVC gas fraction and only weakly with the fraction of IVC gas that on average must have dust content that is not greatly different from “normal”. The reddening per atom varies in the opposite sense with the fraction of gas around 0-velocity, in compensatory fashion. The regression

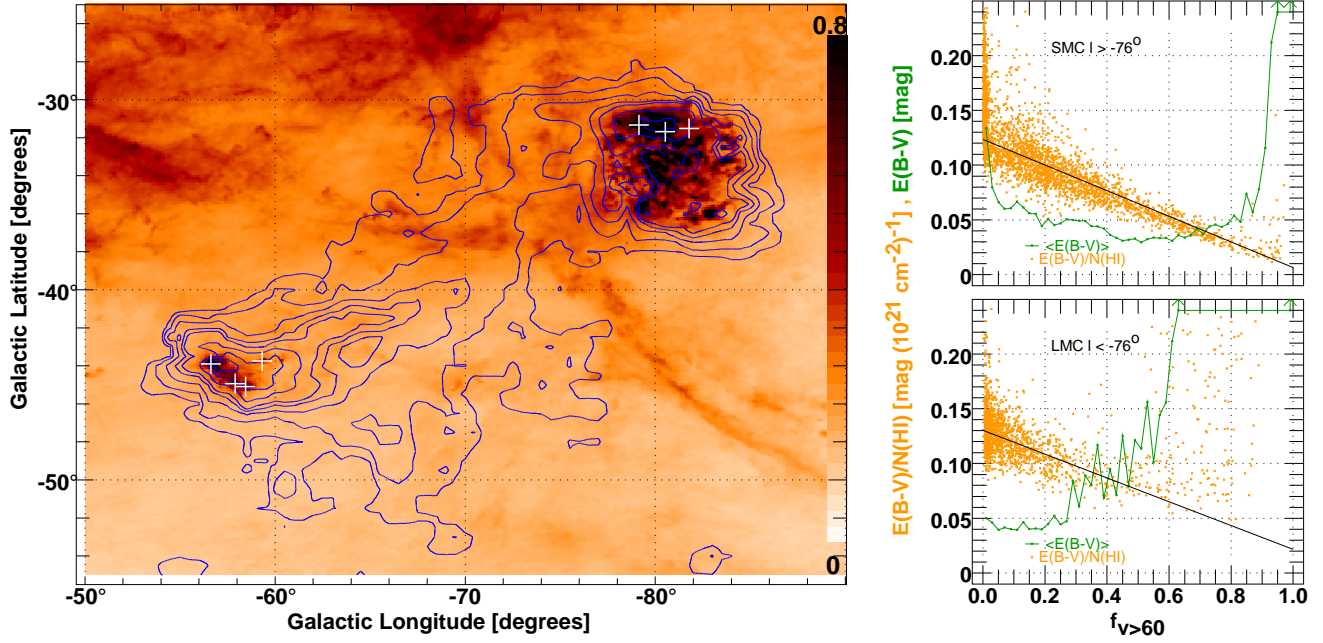


Figure 7. $E(B-V)$, $N(\text{H I})$ and the dust/gas ratio toward the Magellanic Clouds. Left: Contours of $N(\text{H I})$ integrated at $v_{\text{lsr}} \geq 60 \text{ km s}^{-1}$ are shown at levels 1%, 2%, 4%, 7%, 10%, 20%, 40% and 70% of the peak $N(\text{H I}) = 10^{22} \text{ cm}^{-2}$ and overlaid on a pseudocolor rendering of the reddening scaled between 0 and 0.8 mag. The maximum reddenings in the SMC (the peak at $l \simeq -57^\circ$) and LMC are 1.41 and 30.2 mag respectively and the mean reddening along the filament at middle-lower right is 0.07 ± 0.03 mag. White crosses denote regions of CO emission as noted in Section 3.1 Right: Plots of $E(B-V)/N(\text{H I})$ and $\langle E(B-V) \rangle$ relative to the fraction of the integrated $\lambda 21\text{cm}$ H I brightness at $v > 60 \text{ km s}^{-1}$ for the LMC (top) and SMC (bottom). The solid line in each panel at right is a regression line calculated for the data at $\langle E(B-V) \rangle \leq 0.1$ mag.

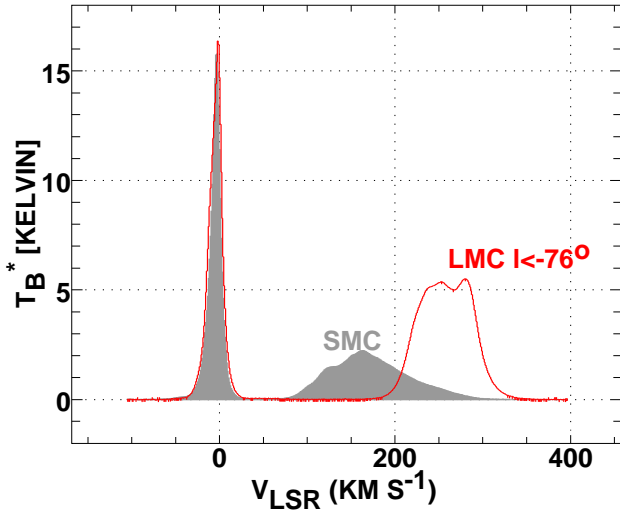


Figure 8. Mean spectra for the SMC ($l \geq -76^\circ$) and LMC ($l < -76^\circ$) for pixels in Figure 7 where $N(\text{H I}) \geq 10^{20} \text{ cm}^{-2}$.

lines intercept the vertical axis near the equivalents of the canonical high Galactic latitude value $N(\text{H I})/E(B-V) \approx 8.3 \times 10^{21} \text{ cm}^{-2} \text{ mag}^{-1}$ for 0 gas fractions in the HVC and IVC components or 100% of the low-velocity (see Table 1 as discussed below).

Figure 6 likewise plots the $E(B-V)/N(\text{H I})$ ratio against the HVC gas fraction across the three HVC complexes C, M, and A, extended over the full range of the horizontal axis. The behavior is similar in all cases, indicating on average very little contribution to $E(B-V)$ from gas at $v \leq -90 \text{ km s}^{-1}$ as inferred from the small values of $E(B-V)/N(\text{H I})$ extrapolated to unit HVC gas fraction. This is quantified in Table 1 as discussed in Section 3.2 with the inclusion of gas seen around the Magellanic Clouds. This is particularly interesting for the region containing HVC Complex M where [Schmelz & Verschuur \(2022\)](#) and [Verschuur & Schmelz \(2023\)](#) have presented a convincing case that the gas kinematics are related

lines intercept the vertical axis near the equivalents of the canonical high Galactic latitude value $N(\text{H I})/E(B-V) \approx 8.3 \times 10^{21} \text{ cm}^{-2} \text{ mag}^{-1}$ for 0 gas fractions in the HVC and IVC components or 100% of the low-velocity (see Table 1 as discussed below). Figure 6 likewise plots the $E(B-V)/N(\text{H I})$ ratio against the HVC gas fraction across the three HVC complexes C, M, and A, extended over the full range of the horizontal axis. The behavior is similar in all cases, indicating on average very little contribution to $E(B-V)$ from gas at $v \leq -90 \text{ km s}^{-1}$ as inferred from the small values of $E(B-V)/N(\text{H I})$ extrapolated to unit HVC gas fraction. This is quantified in Table 1 as discussed in Section 3.2 with the inclusion of gas seen around the Magellanic Clouds. This is particularly interesting for the region containing HVC Complex M where [Schmelz & Verschuur \(2022\)](#) and [Verschuur & Schmelz \(2023\)](#) have presented a convincing case that the gas kinematics are related

to a supernova remnant destroying dust in disk gas that otherwise would be expected to have a normal gas/dust ratio.

3.1. *The Magellanic Clouds*

The region of the sky around the Large and Small Magellanic Clouds (LMC and SMC; Figure 7) presents examples where the gas velocity is at least somewhat associated with identifiable systems whose metallicities have been measured, so the effects of differing metallicity may be explored within the Clouds and in comparison with Milky Way material having Solar metallicity observed in the same directions. Typical metallicities are one-half and one-fifth Solar for the Large and Small Clouds, respectively.

Shown in Figure 7 at left is a map of the H I column density at $v_{\text{lsr}} > 60 \text{ km s}^{-1}$ where the stellar body of the SMC overlays the peak at $l \approx -57^\circ$ and we have indicated regions where Saldaña et al. (2023) mapped CO emission around two positions in the Bar and in N83 and NGC602. $\lambda 21\text{cm}$ H I emission spectra in this portion of the SMC are among the brightest in the entire sky, with a peak $T_{\text{B}} \approx 125 \text{ K}$, presumably because the small metallicity and low dust content of the SMC inhibit the conversion of atomic to molecular hydrogen even with very large gas columns. The LMC overlays the H I and E(B-V) peaks at $l \lesssim -78^\circ$ and the crosses there represent regions where Finn et al. (2022) observed CO emission in the Ridge, 30Dor and N159. Mean spectra illustrating the H I kinematics of both Clouds are shown in Figure 8.

Figure 7 at right shows strong differences in the H I, reddening and dust/gas ratios between the regions on either side of $l = -76^\circ$. The region at $l > -76^\circ$ including the SMC at top right has only very limited regions where $E(\text{B-V}) > 0.05 \text{ mag}$ and the variation of the $E(\text{B-V})/N(\text{H I})$ ratio resembles those shown for the HVC Complexes in Figures 6 and 7 while extending to fractional occupations near unity having very small $E(\text{B-V})/N(\text{H I})$. By contrast, much of the surface area of the H I distribution in the LMC at $l < -76^\circ$ has appreciable red-

dening $E(\text{B-V}) > 0.1 \text{ mag}$ where the dust/gas ratio $E(\text{B-V})/N(\text{H I})$ is at least $2/3$ that of the Galactic gas seen in this portion of the sky. The reddening in regions of very high apparent $E(\text{B-V})$ toward the LMC have been distorted by FIR emission associated with the regions of strong star formation in the LMC. To remove the distortions introduced by star formation, regression fits were limited to pixels with $E(\text{B-V}) < 0.1 \text{ mag}$.

3.2. *Limiting values*

Shown in Table 1 are the limiting values for the gas/dust and dust/gas ratios in the HVC complexes and Magellanic Clouds, derived from the regression lines shown in Figures 6 and 7. The limiting values for unit spectrum occupancy of HVC and Magellanic Cloud gas are typically 5-7 times smaller with a weighted mean difference of a factor 5.3 ± 1.7 . The values extrapolated to 0 spectrum occupation by high-velocity gas cluster around the old value and have a weighted mean $N(\text{H I})/E(\text{B-V}) = 8.3 \pm 0.4 \times 10^{21} \text{ cm}^{-2} \text{ mag}^{-1}$, indicating that the old value was not materially influenced by the presence of low metallicity material.

3.3. *Is E(B-V) reliably estimated in HVC gas?*

The reddening per H-atom assigned to HVC gas by Schlegel et al. (1998) is some five times smaller than for Galactic disk gas (Table 1) and a similar result is found when the reddening is derived from Planck dust opacity measurements (Planck Collaboration XLVIII et al. 2016). Shown at left in Figure 6 and summarized in Table 1 are the $E(\text{B-V})/N(\text{H I})$ values derived toward HVC Complex C by (Shull & Panopoulou 2024) using Planck data. The nominal gradient is slightly steeper but differences in the limiting values are not statistically significant. We conclude that the small reddening per H I in HVC gas is a real physical effect.

4. SUMMARY

The column densities of neutral atomic and molecular hydrogen $N(\text{H I})$ and $N(\text{H}_2)$ were

measured in UV absorption toward 80 early-type stars using the *Copernicus* satellite and a tight relationship was found between $N(\text{H}) = N(\text{H I}) + 2N(\text{H}_2)$ and the photometric reddening, $\langle N(\text{H}) \rangle / \langle E(B-V) \rangle = 5.8 \times 10^{21} \text{ cm}^{-2} \text{ mag}^{-1}$. This ratio of gas column density to dust reddening became an important Milky Way benchmark at Solar metallicity, with many practical applications owing to the relative ease with which $E(B-V)$ can be measured or derived, compared to either or both $N(\text{H I})$ and $N(\text{H}_2)$.

The ratio $N(\text{H I})/E(B-V)$ would be expected to have the same value at low reddening $E(B-V) \lesssim 0.08 \text{ mag}$ where the H_2 fraction is negligible, but a confirmatory determination of the ratio toward stars is complicated by large scatter in the photometric reddening and an independent determination using $N(\text{H I})$ derived from $\lambda 21\text{cm}$ emission and sub-mm/FIR-derived $E(B-V)$ equivalents found a noticeably different value $\langle N(\text{H I}) \rangle / \langle E(B-V) \rangle = 8.3 \times 10^{21} \text{ cm}^{-2} \text{ mag}^{-1}$ at Galactic latitudes above $|b| = 20^\circ$ where sightlines with such low reddening are found.

Observations of $\lambda 21\text{cm}$ H I emission at high Galactic latitude sample gas at large z -height in the disk and gas outside the Galactic disk that is not present along sightlines toward early-type stars that, as a population, have small Galactic scale heights. The gas/reddening ratio determined over long path lengths at high latitude could be affected by including disk gas stripped of dust at large heights in the Milky Way disk or by the inclusion of low-metallicity gas having an intrinsically small dust content outside the disk.

Disk gas and gas external to the disk can be distinguished in H I kinematics. In Figures 1 and 2 we showed that there is a higher proportion of high and intermediate velocity H I along sightlines at $E(B-V) \leq 0.03 \text{ mag}$ having higher $N(\text{H I})/E(B-V)$ ratios (see Table 2). However, the fraction of kinematically-distinguishable gas is too small to explain the 40% larger gas/reddening ratio seen in $\lambda 21\text{cm}$ emission at high latitudes.

That being said, a reddening deficit in high speed gas can manifest itself quite strongly on small scales locally (Figure 3) when the H I gas fraction is large at velocities $|v_{\text{lsr}}| > 90 \text{ km s}^{-1}$. The so-called intermediate velocity H I at $30 \lesssim |v_{\text{lsr}}| \lesssim 90 \text{ km s}^{-1}$ does not have a strong reddening deficit (Figure 5) and Galactic gas at $|v_{\text{lsr}}| \gtrsim 30 \text{ km s}^{-1}$ can appear at latitudes $|b| \lesssim 30^\circ$ through normal Galactic rotation.

We determined the reddening deficit in high speed gas by correlating the reddening per H I $E(B-V)/N(\text{H I})$ with the high speed gas fraction across H I High Velocity Cloud Complexes C, M, and A in Figure 6 and over the region of the Magellanic Clouds and the Magellanic Bridge in Figure 7. As summarized numerically in Table 1 the results are consistent in showing a deficit of a factor 5.3 ± 1.7 in $E(B-V)/N(\text{H I})$ and in confirming the multiplier 8.3 in the previously determined relationship $\langle N(\text{H I}) \rangle / \langle E(B-V) \rangle = 8.3 \times 10^{21} \text{ cm}^{-2} \text{ mag}^{-1}$ using the measures of $N(\text{H I})$ and $E(B-V)$ employed in this work.

The National Radio Astronomy Observatory is a facility of the National Science Foundation operated under contract by Associated Universities, Inc. I thank the referee for helpful comments that clarified some important points.

APPENDIX

Table 1. Limiting values of $E(B-V)/N(\text{H I})$ and $N(\text{H I})/E(B-V)$ ¹

Source	$E(B-V)/N(\text{H I})$	$E(B-V)/N(\text{H I})$	$N(\text{H I})/E(B-V)$
Limit ²	$f = 0$	$f = 1$	$f = 0$
Complex C	0.1186(0.00052)	0.0150(0.0051)	8.43
Complex M	0.1174(0.00036)	0.0263(0.0033)	8.52
Complex A	0.1302(0.00084)	-0.0110(0.0140)	7.68
SMC/Bridge	0.1170(0.00073)	0.0066(0.0020)	8.54
LMC	0.1303(0.00117)	0.0215(0.0067)	7.67
Weighted mean	0.1198(0.00470)	0.0222(0.0072)	8.34
Complex C (Shull & Panopoulou 2024)	0.1283(0.0144)	0.0172 (0.0360)	7.79

¹ $N(\text{H I})$ is expressed in units of $10^{21} \text{ H I cm}^{-2}$ and $E(B-V)$ in mag

² fractions f of $N(\text{H I})$ at $v < -90 \text{ km s}^{-1}$ or $v > 60 \text{ km s}^{-1}$ for HVC and Magellanic Clouds, respectively

A. NUMERICAL VALUES

Numerical values for the data plotted in Figure 1 are given in Table 2. f_{HVC} and f_{IVC} are the fractions of the mean H I profile occupied by HVC and IVC gas at $|v_{\text{lsr}}| > 90 \text{ km s}^{-1}$ and $30 \text{ km s}^{-1} < |v_{\text{lsr}}| < 90 \text{ km s}^{-1}$, respectively. $f(\text{sky})$, $f(E(B-V))$ and $f(N(\text{H I}))$ are the fractions of the sky, aggregate reddening and aggregate H I column density in the reddening bin represented in each row and the cdf are the respectrum cumulative sum of these fractions.

REFERENCES

- Bohlin, R. C., Savage, B. D., & Drake, J. F. 1978, *ApJ*, 224, 132
- Diplas, A. & Savage, B. D. 1994, *ApJ*, 427, 274
- Draine, B. T. & Salpeter, E. E. 1978, *Nature*, 271, 730
- Finn, M. K., Indebetouw, R., Johnson, K. E. et al., *AJ*, 164, 64
- Gillmon, K., Shull, J. M., Tumlinson, J. et al. 2006, *ApJ*, 636, 891
- Hensley, B. S. & Draine, B. T. 2021, *ApJ*, 906, 73
- Kalberla, P. M. W., Burton, W. B., Hartmann, D. et al. 2005, *A&A*, 440, 775
- Lenz, D., Hensley, B. S., & Doré, O. 2017, *ApJ*, 846, 38
- . 2014a, *ApJ*, 780, 10
- Liszt, H. 2014b, *ApJ*, 783, 17
- . 2021, *ApJ*, 908, 127
- Liszt, H. & Gerin, M. 2023, *ApJ*, 943, 172
- Planck Collaboration XLVIII, Aghanim, N., Ashdown, M. et al. 2016, *A&A*, 596, A109
- Saldaño, H. P., Rubio, M., Bolatto, A. D. et al. 2023, *A&A*, 672, A153
- Schlafly, E. F. & Finkbeiner, D. P. 2011, *ApJ*, 737, 103
- Schlegel, D. J., Finkbeiner, D. P., & Davis, M. 1998, *ApJ*, 500, 525
- Schmelz, J. T. & Verschuur, G. L. 2022, *ApJ*, 938, 68
- Seab, C. G. & Shull, J. M. 1983, *ApJ*, 275, 652
- Shull, J. M. & Panopoulou, G. V. 2024, *ApJ*, 961, 204
- Spitzer, L. 1978, *Physical processes in the interstellar medium* (New York Wiley-Interscience, 1978. 333 p.)
- Verschuur, G. L. 1975, *ARA&A*, 13, 257
- Verschuur, G. L. & Schmelz, J. T. 2023, *ApJ*, 943, 161
- Wakker, B. P. 2001, *ApJS* 136, 463

Table 2. Numerical values for the quantities plotted in Figure 1

$E(B-V)$ mag	$ b $ °	$N(\text{H I})/E(B-V)$ $10^{21} \text{ cm}^{-2} \text{ mag}^{-1}$	f_{HVC}^1	f_{IVC}^1	$f(\text{sky})^2$	$f(E(B-V))^2$	$f(\text{H I})^2$	$\text{cdf}(\text{sky})$	$\text{cdf}(E(B-V))$	$\text{cdf}(N(\text{H I}))$
0.0083	57.94	12.654	0.077	0.194	0.0234	0.0057	0.0030	0.0234	0.0057	0.0030
0.0152	61.35	9.6591	0.058	0.183	0.1757	0.0597	0.0418	0.1991	0.0654	0.0448
0.0248	55.82	8.8715	0.043	0.130	0.1575	0.0802	0.0611	0.3566	0.1457	0.1059
0.0348	46.72	8.7065	0.029	0.086	0.1266	0.0886	0.0688	0.4832	0.2343	0.1747
0.0448	40.35	8.6869	0.034	0.072	0.1029	0.0926	0.0720	0.5861	0.3269	0.2467
0.0548	36.01	8.3869	0.023	0.069	0.0836	0.0888	0.0716	0.6697	0.4158	0.3182
0.0648	34.02	8.0507	0.019	0.067	0.0645	0.0777	0.0652	0.7341	0.4935	0.3834
0.0748	33.28	7.8287	0.018	0.059	0.0497	0.0672	0.0580	0.7838	0.5606	0.4414
0.0848	32.91	7.5879	0.019	0.056	0.0380	0.0565	0.0503	0.8218	0.6172	0.4917
0.0948	32.10	7.2661	0.016	0.049	0.0291	0.0462	0.0430	0.8509	0.6634	0.5347
0.1047	31.52	7.0532	0.019	0.046	0.0231	0.0394	0.0377	0.8740	0.7028	0.5724
0.1148	30.66	6.7653	0.020	0.042	0.0167	0.0299	0.0299	0.8907	0.7327	0.6023
0.1250	29.95	6.4681	0.021	0.040	0.0134	0.0249	0.0260	0.9040	0.7576	0.6283
0.1348	30.09	6.2215	0.015	0.040	0.0115	0.0222	0.0241	0.9155	0.7799	0.6525
0.1448	29.75	6.0510	0.025	0.037	0.0096	0.0194	0.0216	0.9251	0.7993	0.6741
0.1549	29.24	5.8634	0.012	0.037	0.0075	0.0158	0.0182	0.9326	0.8150	0.6923
0.1649	29.06	5.6698	0.019	0.041	0.0067	0.0146	0.0173	0.9393	0.8296	0.7096
0.1746	28.19	5.5565	0.022	0.039	0.0058	0.0130	0.0158	0.9451	0.8426	0.7254
0.1849	28.36	5.4019	0.021	0.035	0.0048	0.0111	0.0138	0.9499	0.8536	0.7392
0.1949	28.86	5.2126	0.016	0.036	0.0041	0.0095	0.0124	0.9540	0.8632	0.7516
0.2047	28.49	5.0432	0.010	0.033	0.0034	0.0082	0.0110	0.9574	0.8714	0.7626
0.2152	29.08	4.9869	0.008	0.031	0.0032	0.0079	0.0107	0.9606	0.8793	0.7733
0.2248	28.89	4.7794	0.008	0.033	0.0028	0.0068	0.0097	0.9634	0.8861	0.7830
0.2350	29.23	4.7664	0.036	0.030	0.0028	0.0073	0.0104	0.9662	0.8934	0.7933
0.2448	28.59	4.6846	0.024	0.027	0.0027	0.0072	0.0104	0.9689	0.9007	0.8038
0.2546	28.89	4.7165	0.012	0.026	0.0024	0.0067	0.0097	0.9714	0.9074	0.8134
0.2649	28.78	4.5209	0.011	0.025	0.0023	0.0064	0.0096	0.9737	0.9138	0.8230
0.2749	28.56	4.4069	0.019	0.024	0.0018	0.0051	0.0078	0.9755	0.9189	0.8308
0.2849	27.84	4.2063	0.010	0.026	0.0016	0.0043	0.0069	0.9771	0.9233	0.8378
0.2950	28.14	4.1864	0.018	0.027	0.0016	0.0046	0.0074	0.9787	0.9278	0.8451
0.3050	28.80	4.1222	0.026	0.027	0.0014	0.0042	0.0068	0.9801	0.9320	0.8520
0.3145	28.17	4.3646	0.042	0.016	0.0013	0.0041	0.0064	0.9814	0.9361	0.8584
0.3250	27.17	3.8315	0.011	0.027	0.0011	0.0031	0.0054	0.9825	0.9392	0.8638
0.3348	28.51	3.9258	0.014	0.022	0.0014	0.0041	0.0071	0.9838	0.9433	0.8709
0.3450	28.22	3.8786	0.012	0.016	0.0011	0.0034	0.0059	0.9849	0.9467	0.8767
0.3551	27.08	3.8915	0.009	0.019	0.0009	0.0029	0.0051	0.9858	0.9496	0.8818
0.3649	27.58	3.8488	0.025	0.024	0.0010	0.0031	0.0055	0.9868	0.9527	0.8873
0.3751	26.66	3.5868	0.014	0.024	0.0009	0.0028	0.0052	0.9877	0.9555	0.8925
0.3847	28.21	3.5819	0.012	0.029	0.0007	0.0023	0.0044	0.9884	0.9578	0.8969
0.3949	27.03	3.4079	0.020	0.024	0.0007	0.0022	0.0043	0.9891	0.9600	0.9012
0.4052	28.41	3.5324	0.034	0.015	0.0006	0.0021	0.0041	0.9898	0.9621	0.9053
0.4146	26.98	3.5868	0.005	0.018	0.0005	0.0018	0.0034	0.9903	0.9639	0.9086
0.4249	27.51	3.4885	0.026	0.016	0.0007	0.0024	0.0047	0.9910	0.9664	0.9134
0.4347	26.01	3.3457	0.011	0.023	0.0006	0.0020	0.0041	0.9916	0.9684	0.9175
0.4447	27.30	3.5281	0.075	0.017	0.0005	0.0019	0.0036	0.9921	0.9702	0.9210
0.6423	25.10	2.5448	0.049	0.016	0.0079	0.0298	0.0790	1.0000	1.0000	1.0000

¹ f_{HVC} and f_{IVC} are the fraction of H I in HVC and IVC in each bin² $f(\text{sky})$, $f(E(B-V))$ and $f(\text{H I})$ are the fractions of sky, $E(B-V)$ and $N(\text{H I})$ in each bin